RSC Advances

PAPER

View Article Online
View Journal | View Issue

Cite this: *RSC Adv.*, 2021, **11**, 36617

Thin robust Pd membranes for low-temperature application

Yuyu Ma,†[ab] Meiyi Wang,†[ac] Chunhua Tang,[a] Hui Li,[*a] Jie Fu[*c] and Hengyong Xu[a]

Received 16th August 2021
Accepted 29th October 2021

DOI: 10.1039/d1ra06192e

rsc.li/rsc-advances

It is known that hydrogen embrittlement could result in warping and destruction of pure Pd membranes, which limits the working temperatures to be above 293 °C. This study attempted to investigate the relationship between hydrogen embrittlement resistance and membrane geometry of ultrathin pure Pd membranes of 2.7–6.3 μm thickness. Thin tubular Pd membranes with an o.d. of 4 mm, 6 mm and 12 mm immediately suffered from structural destruction when exposed to H_2 at room temperature. In contrast, thin hollow fiber membranes (outer diameter, 2 mm, thickness < 4 μm) exhibit strong resistance against hydrogen embrittlement at temperatures below 100 °C during repeated heating/cooling cycles at a rate up to 10 °C min^{-1} under H_2 atmosphere. This is ascribed to reduced lattice strain gradients during α–β phase transition in cylindrical structures and lower residual stresses according to *in situ* XRD analysis, which shows a great prospect in low temperature applications.

1. Introduction

Hydrogen embrittlement remains a vital challenge for industrial applications. For example, the high-strength steels looking to use as pressurized hydrogen containers and pipes suffer from hydrogen embrittlement due to hydrogen absorbing at dislocations, grain boundaries or precipitates.[1] Pd, V, Nb, Ta alloy membranes have attracted extensive attention in hydrogen and its isotopes separation, purification and production in membrane reactors, owing to their extraordinary hydrogen permeability and selectivity.[2–5]

The thermal and chemical stability of Pd membranes represent a great challenge for their wide applications, *e.g.* α to β phase transition at temperatures below 573 K and at pressures below 20 bar, leading to large difference in lattice parameters and significant structural deterioration to the membranes,[6–9] and the presence of sulfur-containing species leading to the formation of palladium sulfide species as in the case of zeolite catalysts.[10–13] Several strategies have been developed to improve the stability, *e.g.*, Pd nanoparticles packed inside the porous support to suppress the α to β phase transition,[14,15] and the formation of Pd–Ag, Pd–Cu or Pd/Y alloys.[16,17]

The application of pure Pd membranes often limits its operating temperature above 300 °C.[18–21] There are two phases in the Pd–H system, the one with lower hydrogen content is called α-phase, and the hydrogen-rich phase is usually termed β-phase. When below the critical temperature about 293 °C and at hydrogen pressure < 20 bar, the β-phase nucleates and grows in α-phase and this system is possible for the two phases to coexist.[22–25] The α- and β-phase have the same lattice symmetry but very different volumes, for example, at 25 °C the H/Pd ratio of α-phase is about 0.015, whereas β-phase has $n_H/n_{Pd} \approx 0.7$ at 1 bar.[26,27] When phase transition occurs, the expansion of volume for the phase transition is over 10%, which is accompanied by considerable mechanical stress and leading to the fracture of membrane.[22,28,29]

It is reported that the shear stress generated during the hydrogen absorption process significantly decreases when reducing the radius of the tubular structure.[29] On the other hand, residual stresses, which are defined as stresses remaining in material or body after processing, in the absence of external forces or thermal gradients, can exist after many manufacturing processes involving heat treatment, machining or processing operations. They influence the properties of the component and its lifetime.[30] Moreover, residual stresses play an important role in the crack formation, and they can translate into stress intensity factors acting on cracks that nucleate and propagate around the imperfections.[31] Because of these considerations, this study attempted to fabricate thin Pd membranes on capillary tubular support, which is expected to reduce the internal stress and correlated lattice strain gradients and thus suppress hydrogen embrittlement due to α–β phase transition.

2. Experimental

2.1 Fabrication of the membranes

Porous tubular supports with an outer diameter of 2 mm (porous alumina tubes with an average pore size of 100 nm,

[a]Dalian National Laboratory for Clean Energy, Dalian Institute of Chemical Physics, Chinese Academy of Sciences, Dalian 116023, China. E-mail: hui.li@dicp.ac.cn
[b]University of Chinese Academy of Sciences, Beijing 100049, China
[c]Dalian Jiaotong University, Dalian 116028, China. E-mail: dicpfj@126.com
† These authors contributed equally to this work.

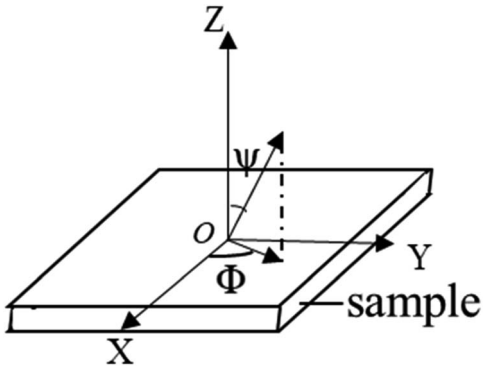

Fig. 1 Graphical representation of the direction and angle of stress.

provided by Prof. Kang Li, Department of Chemical Engineering, Imperial College London, UK), 6 mm (porous stainless steel with an average pore size of 400 nm, from Nanjing Tech University, China) and 12 mm (porous alumina tubes with an average pore size of 100 nm, from Nanjing Tech University, China) were used as membrane substrates. A thin Pd layer was prepared onto the porous support through the modified electroless-plating method (ELP) described previously,[32] which included several steps: (i) modification of the porous substrate with alumina powers, (ii) activation of the support surface through repeated alternate immersion in $SnCl_2$ and $PdCl_2$ solutions; (iii) deposition of Pd with an electroless plating bath containing $PdCl_2$ and EDTA; (iv) thermal treatment at 773 K for 2 h under hydrogen atmosphere.

2.2 Permeation tests

One end of the capillary Pd membrane with a diameter of 2 mm was sealed with epoxy structural adhesive (Ausbond EP2120), while the other end was connected with a stainless steel tube to measure the gas permeation flux. The tubular membranes with a diameter of 6 mm or 12 mm were sealed and mounted into a stainless steel reactor with graphite gaskets, which was located inside a furnace with a programmable temperature controller. The gas pressure was applied at the outer side of membranes. Feed gas flow and pressures were manipulated with a mass flow controller in the feed and a back pressure valve in the retentate side in the range of 10–200 ml min^{-1} and 1–10 bar, respectively. No sweep gas was used during permeation measurements with the permeation side kept at atmospheric pressure. The main tests are listed as below:

(1) Thin tubular Pd membranes on porous support with a diameter of 2 mm (denoted as P-2), 4 mm (denoted as P-4), 6 mm (denoted as P-6) and 12 mm (denoted as P-12), respectively, were exposed to H_2 at room temperature to evaluate the hydrogen resistance with pressure differential alternating between 1 bar and 4 bar.

(2) P-2 and P-4 were tested under repeated heating/cooling cycles between room temperature and 100 °C under a hydrogen atmosphere at a feed/permeate pressure differential up to 10 bar.

(3) To investigate the phase transition of P-6 at higher pressures, the feed pressure was increased from 2 bar to 10 bar while the permeate pressure remained as 1 bar with increasing the temperature from 200 °C to 400 °C.

The membrane surface and cross-sectional analysis of P-2 were carried out using scanning electron microscopy (SEM, JSM-7800F) equipped with energy-dispersive X-ray spectroscopy (EDX). The *in situ* X-ray diffraction patterns were analyzed using Empyrean-100. The stress was analyzed by X-ray Powder Diffractometer – SmartLab.

The method of measuring residual stresses with XRD is based on the measurement of lattice strains by studying the variations of lattice spacing induced by compressive or tensile stresses and to calculate the stresses from the strains.[33] The $\sin^2\psi$ method can determine the stress in any direction along the plane *XY* (Fig. 1), and when the angle ψ between the normal of the sample and the normal of the diffracting plane changes, the diffraction angle 2θ of the plane will also change.[21] Therefore, the measurement of planes at an angle ψ can be made by changing the tilt of the sample within the diffractometer, and the strains along that direction can be calculated from the variation of lattice spacing d: d_0, determined by the position of the Bragg peak of stressed (θ) and stress-free (θ_0) material:

$$\varepsilon = \frac{d - d_0}{d_0} \quad (1)$$

The direction Φ is the angle between a direction fixed in the plane and the projection of the normal to the plane of diffraction in that plane. Using the strains to evaluate the stress σ_ϕ, which can be given by:

$$\sigma_\phi = \frac{E}{(1+\upsilon)\sin^2\psi}\frac{d_\varphi - d_z}{d_z} = KM \quad (2)$$

E and υ denote Young's modulus and Poisson's ratio, is d_φ is the inter-planar spacing of planes at an angle ψ to the surface and d_z is the inter-planar spacing of planes normal to the surface.

Table 1 Performance data of the membranes investigated in this study

Diameter (mm)	Porous support	Thickness (μm)	N_2 flux[a] (mol s^{-1} m^{-2})	N_2 flux[b] (mol s^{-1} m^{-2})	Multiple
2.00	Alumina	4.00	2.12×10^{-10}	3.72×10^{-11}	0.18
2.00	Alumina	2.70	2.70×10^{-10}	3.12×10^{-10}	1.16
4.00	Alumina	3.50	7.69×10^{-9}	1.66×10^{-8}	2.16
6.00	Stainless-steel	3.90	4.43×10^{-10}	1.10×10^{-8}	24.86
12.00	Alumina	6.30	1.25×10^{-9}	2.02×10^{-8}	16.15

[a] Before feeding hydrogen. [b] After feeding hydrogen.

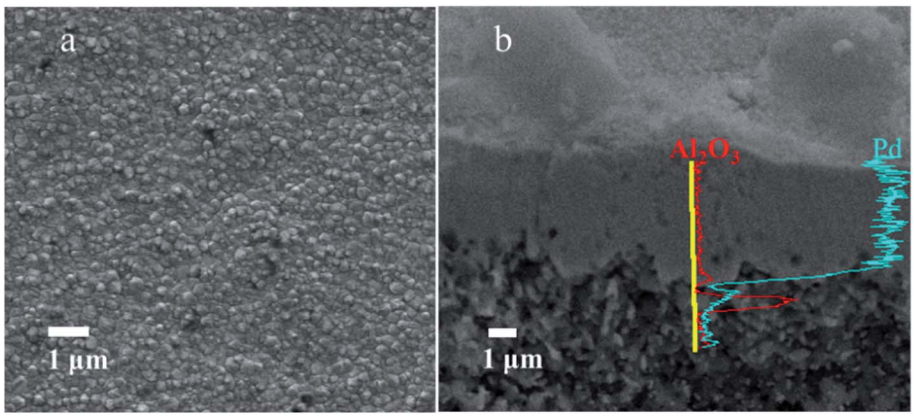

Fig. 2 (a) SEM images of P-2 surface and (b) energy-dispersive X-ray (EDX) spectroscopy line analysis of the cross section.

3. Results and discussion

3.1 Investigation of hydrogen embrittlement resistance at low temperatures

As mentioned above, P-2, P-4, P-6 and P-12, were exposed to H_2 at room temperature to evaluate the hydrogen resistance with pressure differential alternating between 1 bar and 4 bar (Table 1). It can be seen from Table 1 that the N_2 leak rate of P-6 and P-12 increased about 16–24 times immediately after exposure to H_2, indicating fracture of membranes. On the contrary, the N_2 flux of the P-4 only increased slightly and the P-2 remained almost unchanged, implying a strong resistance to hydrogen embrittlement. Fig. 2 shows surface and cross-sectional images of P-2, which exhibits a dense membrane surface and homogeneous thickness. No pinholes or micro pores can be observed from the images. There appear Pd grains on the membrane surface which represents the typical morphology of Pd membranes fabricated *via* electroless-plating approach.

To further investigate the hydrogen embrittlement resistance of P-4 and P-2, it was tested under repeated heating/cooling cycles between room temperature and 100 °C under a hydrogen atmosphere at a feed/permeate pressure differential up to 10 bar. The N_2 leak rate was measured at a 4.5 bar pressure differential between the temperature cycles as shown in Fig. 3 to evaluate the integrity of the membrane. It can be seen that both H_2 and N_2 flux of P-2 remained stable after 8 repeated cycles, after exposure to hydrogen atmosphere below 100 °C for about 157 h in total, while N_2 flux of P-4 increased steadily and tripled after 6 cycles. Note that the H_2 flux obtained was at an appreciable level of 10^{-7} mol s^{-1} m^{-2} Pa^{-1} under the operating temperature of 100 °C and 10 bar pressure differential, which exhibits great prospects for low-temperature applications.

Meanwhile, as shown in Fig. 4, the surface morphology of P-2 before and after heating/cooling cycles is basically unchanged, and there is no major change in the surface grain size (Fig. 4a and b).

Subsequently, *in situ* XRD analysis was carried out to clarify the different behavior of these tubular membranes in the coexistence of α and β phase at room temperatures. The scanning procedure is as below: the scan was first conducted under N_2 atmosphere, and then switched to H_2 atmosphere, with each scan lasting for 1.5 min. Fig. 5 shows the *in situ* XRD patterns of Pd membranes with a diameter of 2 mm, 6 mm, and 12 mm, respectively. Peaks appearing on the right correspond to (111) of

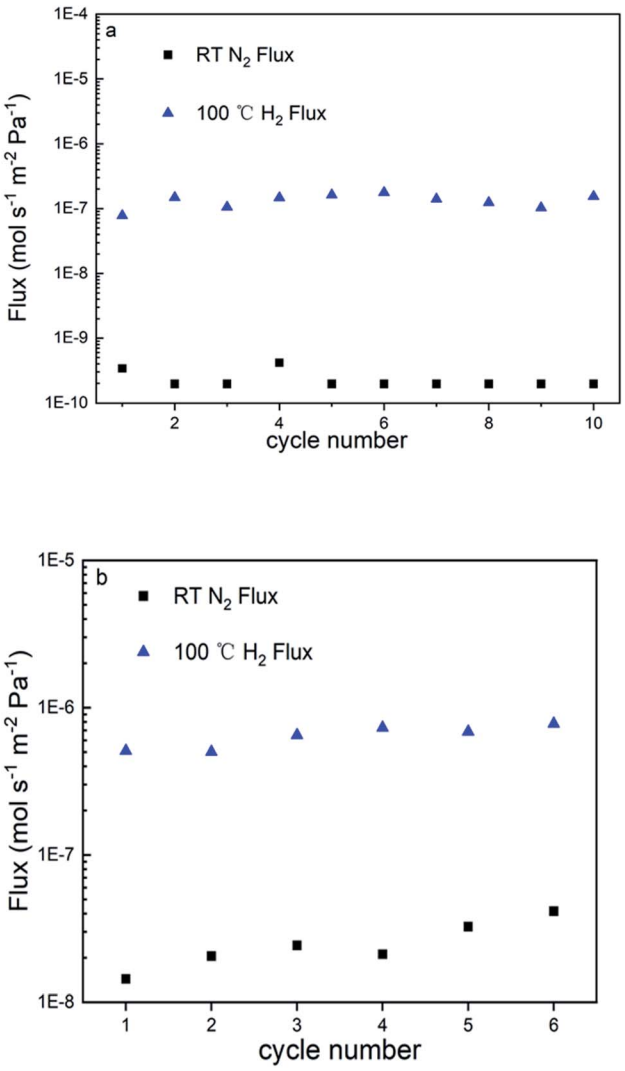

Fig. 3 H_2 and N_2 flux of (a) P-2, (b) P-4 during repeated heating/cooling cycles between room temperature and 100 °C at a pressure differential up to 10 bar.

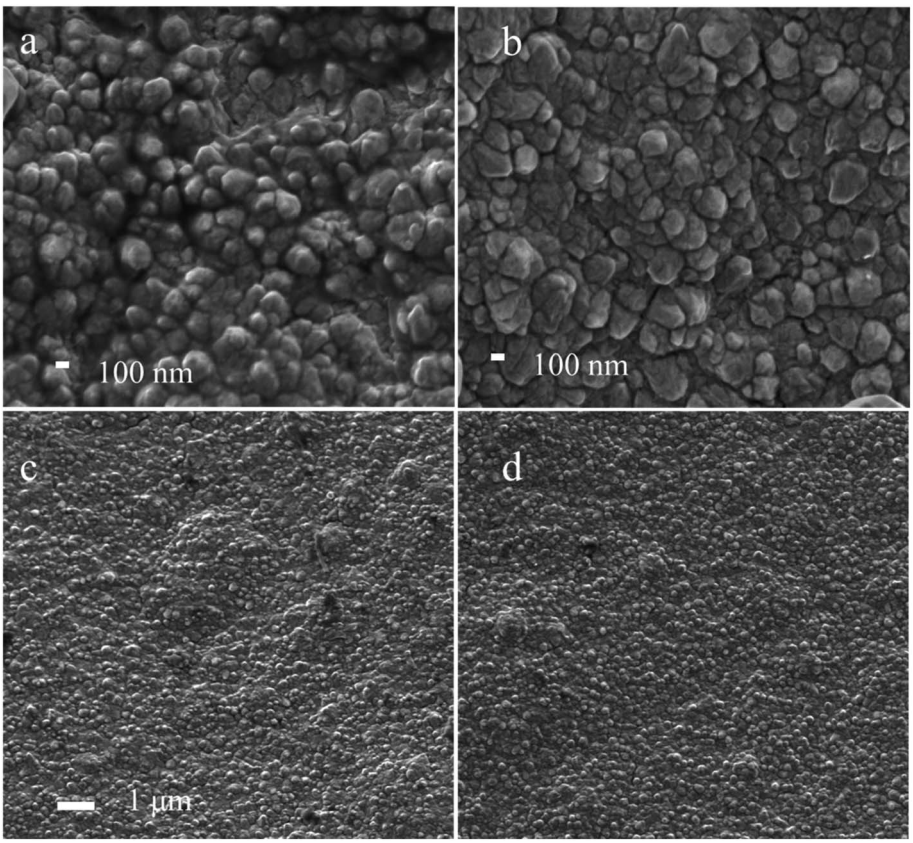

Fig. 4 SEM images of P-2 surface (a) and (c) before heating/cooling cycles, (b) and (d) after heating/cooling cycles.

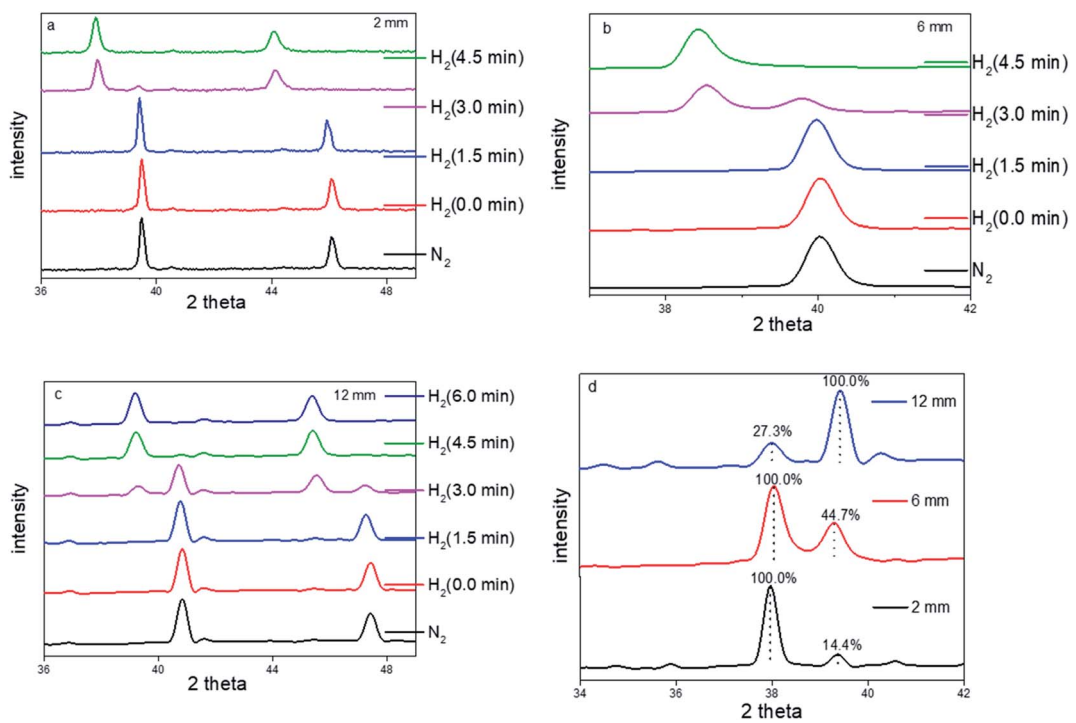

Fig. 5 *In situ* XRD patterns of (a) P-2, (b) P-6 and (c) P-12 at room temperature when exposed to N_2 and H_2 atmosphere. (d) Comparison of the intensity of the α-phase and β-phase peaks of P-2, P-6 and P-12 at the third minute.

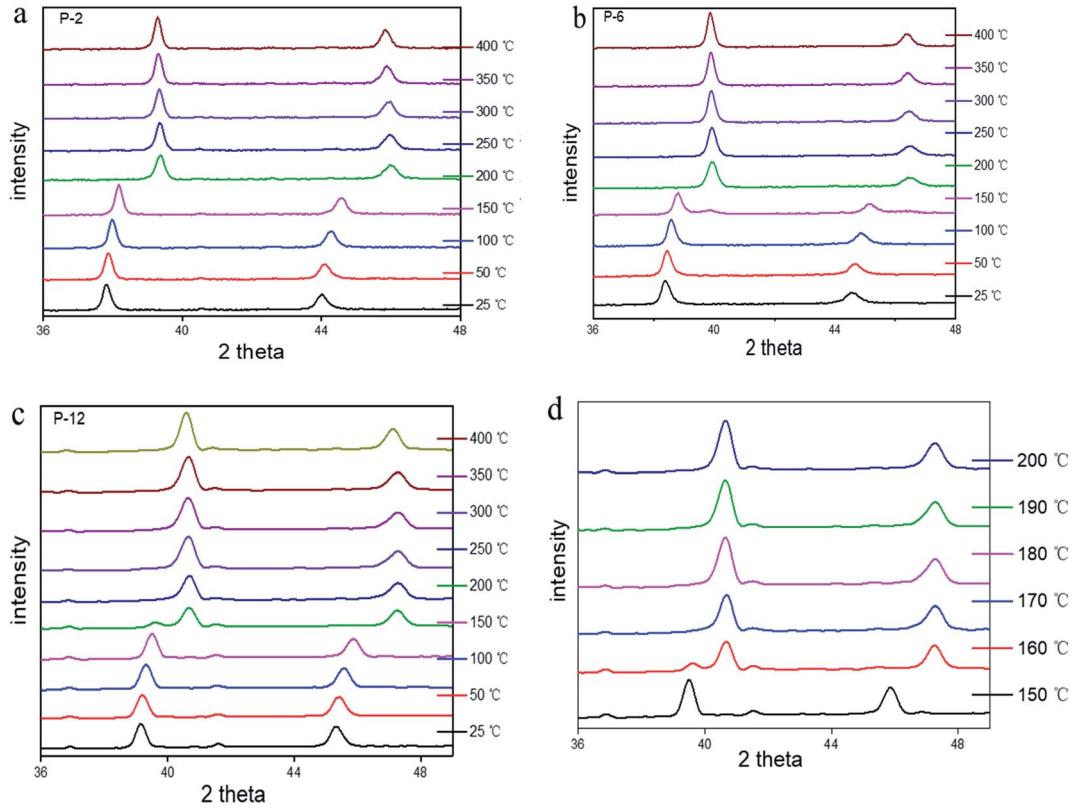

Fig. 6 Phase transition temperatures of membranes with different diameters (a–d) at a feed pressure of 2 bar between 25 °C and 400 °C.

Pd and α-phase, and the peaks on the left can be indexed to β-phase. Interestingly, it is found that the peaks of α-phase of P-2 and P-6 completely disappeared after 4.5 min of feeding hydrogen whereas that of P-12 disappeared after 6 min of feeding hydrogen. Fig. 5d shows the comparison of the peak intensities of P-2, P-6 and P-12 at 3rd min, which can be seen that the α-phase of P-2 is only 14.4% of the β-phase, the α-phase of P-6 is 44.7% of the β-phase, and the β-phase of P-12 is only 27.3% of the α-phase, implying that it takes a longer time to complete phase transition as to P-6 and P-12 than P-2.

It is known that the coexistence of two unequal phases with different specific volume causes internal stress.[2] Since P-2 completes the α–β phase transition at the highest rate, the risk of lattice distortion due to internal stresses is diminished. This provides an explanation for the strong resistance of thin tubular P-2 in the coexistence of α and β phase, *i.e.*, the internal stress is significantly suppressed due to a faster phase transition process with the decrease of the radius. The hydrogen embrittlement resistance of thin hollow fiber Pd membranes, as compared to conventional tubular membranes, is attributed to tubular structure effects originating from the suppressed internal stress, which coincides with modeling studies.[29]

Fig. 6a–c shows that the phase transition of pure Pd membranes occur in the temperature range of 150 °C to 200 °C at a feed pressure of 2 bar which has no relation to varying diameters, *i.e.* 2 mm, 6 mm and 12 mm. Fig. 6d indicates that the β–α phase transition is completed at temperatures above 170 °C for these membranes. Further detailed analysis (Fig. 7) shows that the peak change is completed at 150 °C for P-2 while there is certain α phase remaining as to P-6 at 150 °C, corroborating the faster phase transition process and shorter-term coexistence of two phases in P-2 with a lower diameter.

3.2 The phase transition investigation of P-6 at varying temperatures and pressures

It is known from above that the phase transition for P-2, P-6 and P-12 occurs at temperatures below 200 °C at a feed pressure of 2 bar, implying that these membranes can avoid destruction in H_2 atmosphere at temperatures above 200 °C. Fig. 8 indicates that both H_2 and N_2 permeation of P-6 remained at a steady level during 8 repeated cycles between 200 and 400 °C under H_2 atmosphere, except the slight increase after the first cycle. This observation confirmed the above results.

To further investigate the phase transition of P-6 at higher pressures, the feed pressure was increased from 2 bar to 10 bar while the permeate pressure remained as 1 bar. Fig. 9 shows the activation energy of H_2 permeation between 200 °C and 400 °C at a feed/permeate pressure of 10/1 bar, which exhibits two stages in the temperature range of 200–250 °C and 250–400 °C. Note that the N_2 permeation of P-6 tripled during the following 10 repeated cycles between 200 °C and 400 °C, while an obvious increase in N_2 permeation was observed after only 4 repeated cycles between RT and 400 °C (Fig. 10). This implies the hydrogen embrittlement resistance at temperatures above 200 °C for P-6 even at a high feed pressure of 10 bar.

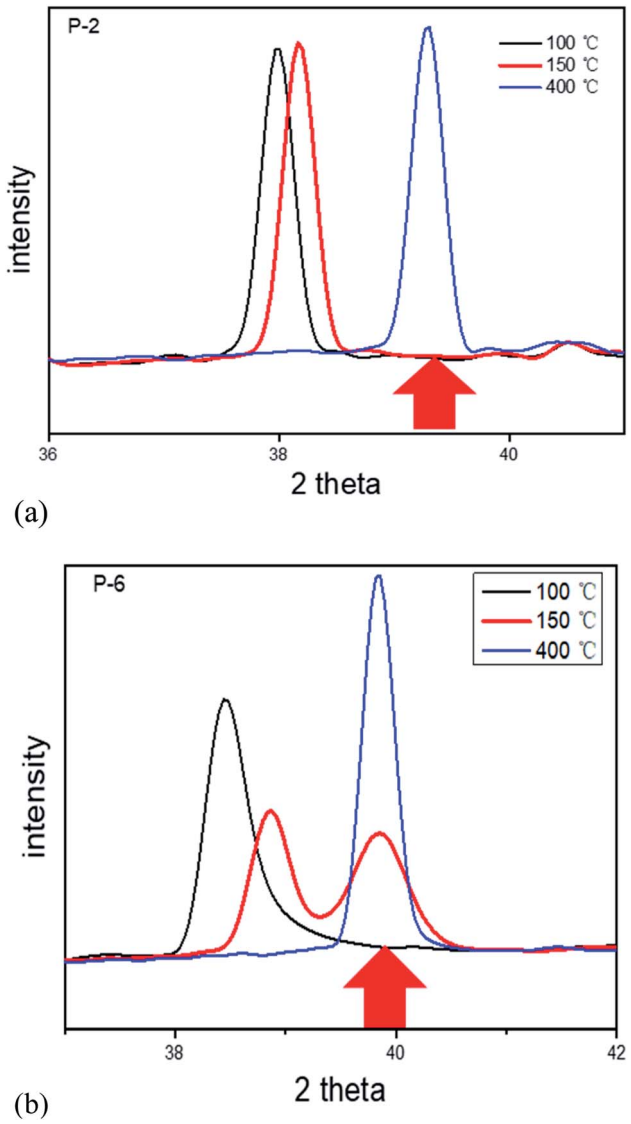

Fig. 7 Peak change at 100 °C, 150 °C and 400 °C for (a) P-2 and (b) P-6.

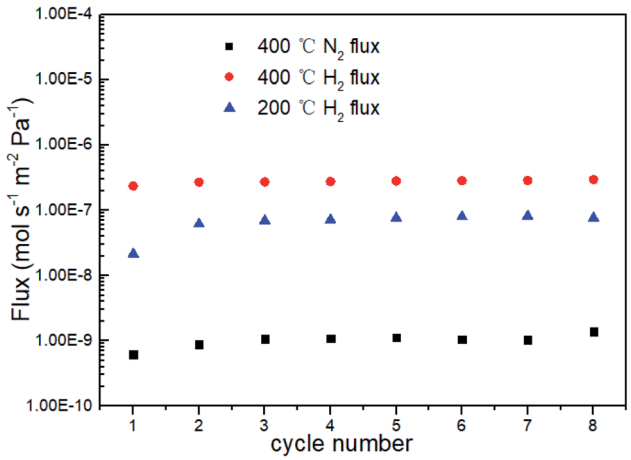

Fig. 8 H_2 and N_2 flux of P-6 during repeated heating/cooling cycles between 200 °C and 400 °C at a pressure differential of 1 bar.

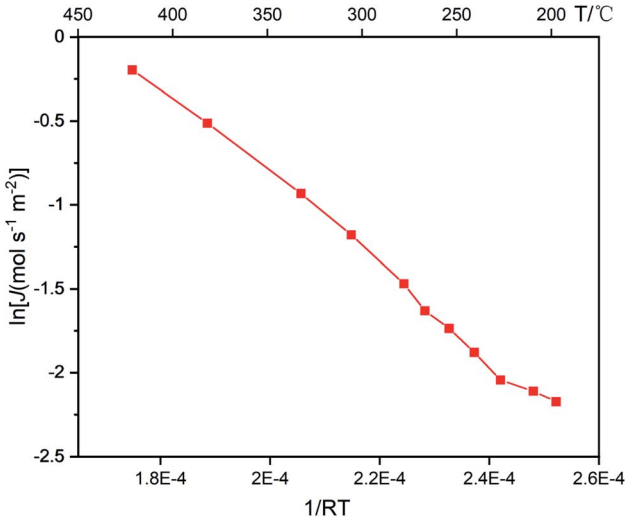

Fig. 9 Activation energy curve of P-6 at a pressure differential of 9 bar between 200 °C and 400 °C.

3.3 Residual stress measurement

To determine the diffraction crystal plane, a wide-angle scan of the sample was performed, as shown in Fig. 11. Considering the peak intensity and face spacing errors, the (311) face was selected as the diffraction crystal face and the scan range is 80.5–84° in this study.

According to the equation for stress measurement by XRD method (eqn (2)), the stress σ_ϕ can be obtained from the slope of the line by measuring the diffraction line displacement at multiple ψ angles and using 2θ as the vertical coordinate and sin as the horizontal coordinate to calculate and plot the line closest to each experimental value using the least squares. ψ angles are taken as 0°, 17°, 25°, 30°, 35°, 40°, 45° respectively, Young's modulus E takes 117 GPa and Poisson's ratio υ takes 0.39 (from MatWeb). The results of P-2 and P-4 are plotted in Fig. 12, and the residual stress of P-2 is 248.91 MPa with an uncertainty of ±23.86, and that of P-4 is 701.66 MPa with an

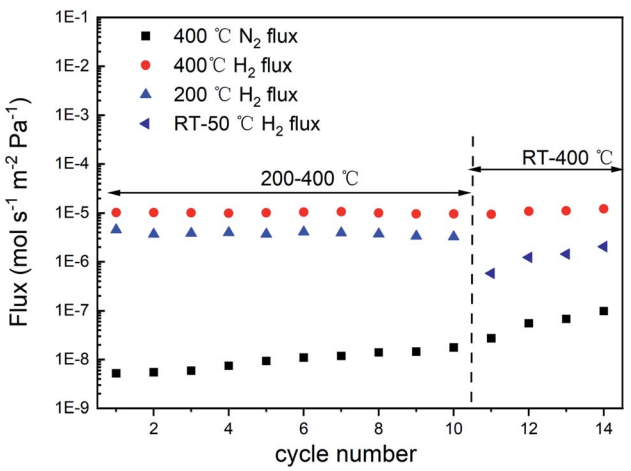

Fig. 10 H_2 and N_2 flux of P-6 during repeated heating/cooling cycles between 200 °C/RT and 400 °C at a pressure differential of 9 bar.

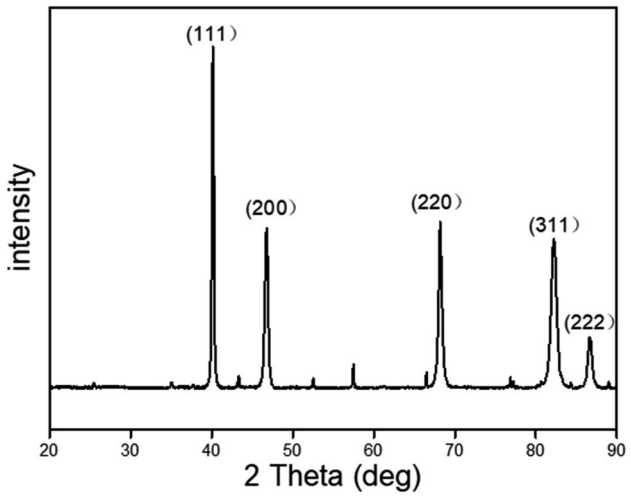

Fig. 11 X-ray diffraction pattern of palladium membrane.

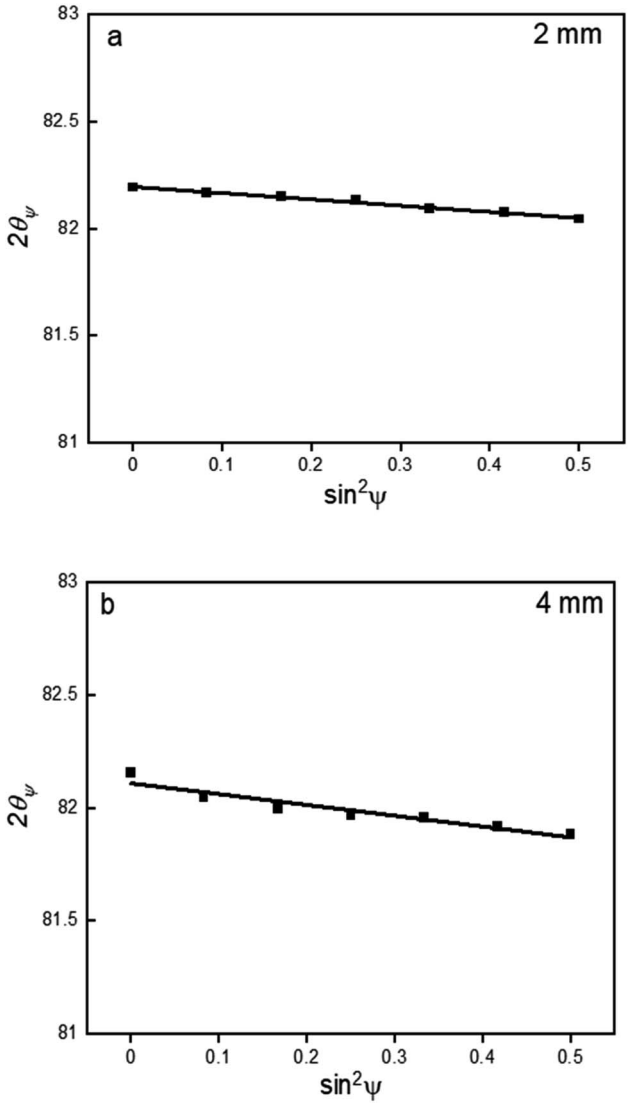

Fig. 12 Graphical plot of 2θ as a function of $\sin^2\psi$ for (a) P-2 (b) P-4, both exhibiting a negative slope.

uncertainty of ±57.47. It is observed from Fig. 12 that P-2 and P-4 show tensile stress and the value of P-4 is greater than P-2, which means that P-2 is more resistant to fatigue than P-4.[34] Given that the other fabrication conditions of P-2 and P-4 are the same, the greater tensile stress in P-4 than in P-2 is attributed to the difference in diameter. This may offer a new route for the development of metal materials against hydrogen embrittlement from the structural design point of view.

4. Conclusions

Thin hollow fiber Pd membranes (o.d. 2 mm, thickness < 4 μm) show strong resistance against α–β phase transition at temperatures between room temperature and 100 °C, and Pd membrane with a diameter of 4 mm also exhibits some degree of resistance to hydrogen embrittlement in this temperature range, whereas tubular membranes with an increased diameter of 6 mm and 12 mm immediately suffered from hydrogen embrittlement upon hydrogen exposure at room temperature.

In situ XRD analysis indicates a faster phase transition process and shorter-term coexistence of two phases in Pd membranes with a lower diameter. On the other hand, the stress measurement by XRD method presents a higher tensile stress for Pd membranes with a higher diameter. This is ascribed to reduced internal stress and lattice strain gradients with the decrease of the radius in cylindrical structures and lower residual stress, which may provide a route for the suppression of hydrogen embrittlement of other metal materials.

Conflicts of interest

There are no conflicts to declare.

Acknowledgements

We are grateful for the financial support from National Natural Science Foundation of China (Grant No. 21676265; 51501177; 21306183), and the K. C. Wong Education Foundation (GJTD-2018-06). We are in debt to Prof. Kang Li from Imperial College London for his kind support with porous capillary tubes.

References

1 Y. S. Chen, H. Z. Lu, J. T. Liang, A. Rosenthal, H. W. Liu, G. Sneddon, I. McCarroll, Z. Z. Zhao, W. Li, A. M. Guo and J. M. Cairney, Observation of hydrogen trapping at dislocations, grain boundaries, and precipitates, *Science*, 2020, **367**(6474), 171–175.
2 S. N. Paglieri and J. D. Way, Innovations in palladium membrane research, *Sep. Purif. Methods*, 2002, **31**(1), 1–169.
3 S. Yun and S. T. Oyama, Correlations in palladium membranes for hydrogen separation: a review, *J. Membr. Sci.*, 2011, **375**(1–2), 28–45.
4 V. N. Alimov, A. O. Busnyuk, M. E. Notkin and A. I. Livshits, Pd-V-Pd composite membranes: hydrogen transport in

a wide pressure range and mechanical stability, *J. Membr. Sci.*, 2014, **457**, 103–112.

5 E. H. Yan, H. R. Huang, S. H. Sun, Y. J. Zou, H. L. Chu and L. X. Sun, Development of Nb-Ti-Co alloy for high-performance hydrogen separating membrane, *J. Membr. Sci.*, 2018, **565**, 411–424.

6 M. D. Dolan, Non-Pd BCC alloy membranes for industrial hydrogen separation, *J. Membr. Sci.*, 2010, **362**(1–2), 12–28.

7 F. Gallucci, E. Fernandez, P. Corengia and M. V. Annaland, Recent advances on membranes and membrane reactors for hydrogen production, *Chem. Eng. Sci.*, 2013, **92**, 40–66.

8 F. A. Lewis, The palladium-hydrogen system: structures near phase transition and critical points, *Int. J. Hydrogen Energy*, 1995, **20**(7), 587–592.

9 H. Li, A. Caravella and H. Y. Xu, Recent progress in Pd-based composite membranes, *J. Mater. Chem. A*, 2016, **4**, 14069–14094.

10 N. Pomerantz and Y. H. Ma, Effect of H_2S on the Performance and Long-Term Stability of Pd/Cu Membranes, *Ind. Eng. Chem. Res.*, 2009, **48**(8), 4030–4039.

11 T. A. Peters, T. Kaleta, M. Stange and R. Bredesen, Hydrogen transport through a selection of thin Pd-alloy membranes: membrane stability, H_2S inhibition, and flux recovery in hydrogen and simulated WGS mixtures, *Catal. Today*, 2012, **193**(1), 8–19.

12 T. A. Saleh, Characterization, determination and elimination technologies for sulfur from petroleum: toward cleaner fuel and a safe environment, *Trends Environ. Anal. Chem.*, 2020, **25**, 1588–2214.

13 I. Ali, E. N. Al-Shafei, A. A. Al-Arfaj and T. A. Saleh, Influence of titanium oxide on the performance of molybdenum catalysts loaded on zeolite toward hydrodesulfurization reactions, *Microporous Mesoporous Mater.*, 2020, **303**, 1387–1811.

14 D. A. Pacheco Tanaka, M. A. Llosa Tanco, T. Nagase, J. Okazaki, Y. Wakui, F. Mizukami and T. M. Suzuki, Fabrication of hydrogen-permeable composite membranes packed with palladium nanoparticles, *Adv. Mater.*, 2006, **18**, 630–632.

15 T. Kuji, Y. Matsumura, H. Uchida and T. Aizawa, Hydrogen absorption of nanocrystalline palladium, *J. Alloys Compd.*, 2002, **330–332**, 718–722.

16 K. J. Bryden and J. Y. Ying, Thermal stability and hydrogen absorption characteristics of palladium-yttrium nanoalloys, *Acta Mater.*, 1996, **44**(9), 3847–3854.

17 S. Uemiya, W. Kato, A. Uyama, M. Kajiwara, T. Kojima and E. Kikuchi, Separation of hydrogen from gas mixtures using supported platinum-group metal membranes, *Sep. Purif. Technol.*, 2001, **22–23**, 309–317.

18 L. Zheng, H. Li and H. Xu, "Defect-free" interlayer with a smooth surface and controlled pore-mouth size for thin and thermally stable Pd composite membranes, *Int. J. Hydrogen Energy*, 2016, **41**(2), 1002–1009.

19 Z. Y. Zhang, S. Liguori, T. F. Fuerst, J. D. Way and C. A. Wolden, Efficient Ammonia Decomposition in a Catalytic Membrane Reactor To Enable Hydrogen Storage and Utilization, *ACS Sustainable Chem. Eng.*, 2019, **7**(6), 5975–5985.

20 S. T. B. Lundin, N. S. Patki, T. F. Fuerst, C. A. Wolden and J. D. Way, Inhibition of hydrogen flux in palladium membranes by pressure-induced restructuring of the membrane surface, *J. Membr. Sci.*, 2017, **535**, 70–78.

21 J. H. Lee, J. Y. Han, K. M. Kim, S. K. Ryi and D. W. Kim, Development of homogeneous Pd-Ag alloy membrane formed on porous stainless steel by multi-layered films and Ag-upfilling heat treatment, *J. Membr. Sci.*, 2015, **492**, 242–248.

22 F. D. Manchester, A. San-Martin and J. M. Pitre, The H-Pd (hydrogen-palladium) System, *J. Phase Equilib.*, 1994, **15**(1), 62–83.

23 G. Bellanger, Embrittlement of Palladium and Palladium Silver Alloy Cathode Membranes by Tritium, *Fusion Technol.*, 1995, **27**(1), 36–45.

24 L. J. Gillespie and F. P. Hall, The Palladium-Hydrogen Equilibrium and Palladium Hydride1, *J. Am. Chem. Soc.*, 1926, **48**(5), 1207–1219.

25 Y. Sakamoto, K. Yuwasa and K. Hirayama, X-ray investigation of the absorption of hydrogen by several palladium and nickel solid solution alloys, *J. Less-Common Met.*, 1982, **88**(1), 115–124.

26 F. A. Lewis and S. G. McKee, Hydride Formation by Nickel, Palladium and Platinum, in *Metal–Hydrogen Systems*, ed. VeziroĞLu T. N., Pergamon, 1982, pp. 423–436.

27 E. A. Owen and J. I. Jones, The Palladium-Hydrogen System, *Proc. Phys. Soc.*, 1991, **49**(5), 603–610.

28 J. Shu, B. P. A. Grandjean, A. Vanneste and S. Kaliaguine, Catalytic Palladium-Based Membrane Reactors – a Review, *Can. J. Chem. Eng.*, 1991, **69**(5), 1036–1060.

29 J. C. M. Li, Physical chemistry of some microstructural phenomena, *Metall. Mater. Trans. A*, 1978, **9**(10), 1353–1380.

30 F. Foadian, A. Carradó and H. Palkowski, Precision tube production: influencing the eccentricity and residual stresses by tilting and shifting, *J. Mater. Process. Technol.*, 2015, **222**, 155–162.

31 A. G. Evans, D. R. Mumm, J. W. Hutchinson, G. H. Meier and F. S. Pettit, Mechanisms controlling the durability of thermal barrier coatings, *Prog. Mater. Sci.*, 2001, **46**(5), 505–553.

32 J. X. Liu, X. H. Ju, C. H. Tang, L. Liu, H. Li and P. Chen, High performance stainless-steel supported Pd membranes with a finger-like and gap structure and its application in NH_3 decomposition membrane reactor, *Chem. Eng. J.*, 2020, **388**, 1385–8947.

33 R. Montanari, A. Fava and G. Barbieri, Experimental Techniques to Investigate Residual Stress in Joints, in *Residual Stress Analysis on Welded Joints by Means of Numerical Simulation and Experiments*, 2018, pp. 16–18.

34 V. K. Sinha and V. S. Godaba, Residual stress measurement in worked and heat treated steel by X-ray diffractometry, *Mater. Sci. Eng., A*, 2008, **488**(1–2), 491–495.